ACS OMEGA

http://pubs.acs.org/journal/acsodf

Article

Atomic-Layer-Deposited Aluminum Oxide Thin Films Probed with X-ray Scattering and Compared to Molecular Dynamics and Density Functional Theory Models

Anthony Pugliese, Badri Shyam, Gil M. Repa, Anh Hung Nguyen, Apurva Mehta, Edmund B. Webb III,* Lisa A. Fredin,* and Nicholas C. Strandwitz*

Cite This: *ACS Omega* 2022, 7, 41033−41043

Read Online

ACCESS | Metrics & More | Article Recommendations | Supporting Information

ABSTRACT: A better understanding of amorphous aluminum oxide's structure and electronic properties is obtained through combined experimental and computational approaches. Grazing incidence X-ray scattering measurements were carried out on aluminum oxide thin films grown using thermal atomic layer deposition. The corresponding pair distribution functions (PDFs) showed structures similar to previously reported PDFs of solid-state amorphous alumina and molten alumina. Structural models based on crystalline alumina polymorphs (PDFgui) and amorphous alumina (molecular dynamics, MD) were examined for structural comparisons to the experimental PDF data. Smaller MD models were optimized and verified against larger models to allow for quantum chemical electronic structure calculations. The electronic structure of the amorphous alumina models yields additional insight into the band structure and electronic defects present in amorphous alumina that are not present in crystalline samples.

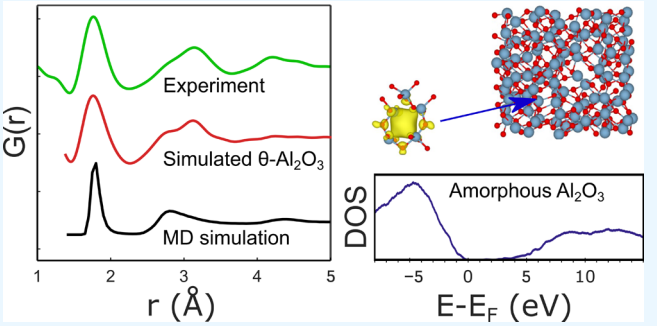

INTRODUCTION

Atomic-layer-deposited (ALD) alumina is a ubiquitous material in scientific studies and is present in many applications, for example, as surface passivation layers,[1,2] diffusion barriers,[3,4] and dielectric layers.[5,6] Alumina is arguably the most-deposited ALD material, not only due to its good properties as a dielectric and physical barrier but also because of the robust growth chemistry of the trimethylaluminum (TMA)−water process.[7,8] The structure and chemistry of ALD alumina films will dictate the physical properties, such as band gap, defect levels, chemical stability, catalytic behavior, etc.; however, short- and medium-range ordered ALD alumina films are difficult to probe, and the structural evolution near crystallization temperatures is not well understood.

Most ALD alumina films do not show long-range order in X-ray and electron diffraction experiments. However, crystallinity in ALD alumina films is of interest, as the long-range order of crystalline alumina films provides insight into short- and medium-range order in amorphous films. Factors that determine if ALD alumina films will be crystalline include deposition temperature, precursor chemistry, substrate choice, and postdeposition processing.[9] Special cases of the direct growth of crystalline alumina phases using ALD include growth on nanowires,[10,11] which results in crystalline alumina in the as-deposited state. Additionally, ALD on $SrTiO_3$ can result in the direct growth of crystalline alumina.[12] High substrate temperatures can be employed using the $AlCl_3$ and water process due to the high thermal stability of the chloride precursor, in which case crystalline films can be obtained.[13] However, the vast majority of ALD alumina films are grown using TMA coupled with an oxygen precursor (water, ozone, or oxygen plasma) under conditions that result in amorphous films, with the upper limit of the deposition temperature dictated by the decomposition temperature of TMA. Postdeposition annealing of amorphous alumina films at or above 900−1050 °C results in crystallization.[14−19] In these prior studies, phases observed after the postdeposition annealing of ALD alumina typically begin with one or more "transition" alumina phases and terminate at the highest temperatures in the α-Al_2O_3 phase.

The composition of ALD alumina is not strictly stoichiometric Al_2O_3 but is more accurately described as $Al_2O_x(OH)_{6-2x}$, sometimes with small amounts of carbon impurities. When grown using the TMA-water process, ALD

Received: July 12, 2022
Accepted: October 12, 2022
Published: November 4, 2022

Table 1. Summary of Structural Data for Amorphous and Molten Aluminum Oxides

technique[a]	sample[b]	R_C (Å)	$\overline{CN}_{Al}$	$\overline{CN}_{O}$	$^{[3]}$Al	$^{[4]}$Al	$^{[5]}$Al	$^{[6]}$Al	ref
N- and X-PDF, RMC	molten	2.5	4.40	2.9	3.5	58	35	4.3	30
N-PDF, EPSR	molten		4.20	2.7	12	62	24	2	33
SS-NMR	sputtered film		4.48			55	42	3	42
SS-NMR	PEALD film		4.51			54	41	5.1	43
X-PDF, RMC	ALD film on CNT	2.2	4.67	2.88					25
e-PDF, RMC	ALD film on CNT		4.97	3					31
MD, melt quench		2.2	4.24	2.83	0.1	77	21	1.6	this work
MD, melt quench		2.5	4.41	2.94	0	65	30	5.4	this work

[a]N-PDF = neutron PDF; X-PDF = X-ray PDF; SS-NMR = solid-state nuclear magnetic resonance; EPSR = empirical potential structure refinement; CNT = carbon nanotube; and MD = molecular dynamics. [b]Indicates whether experimental data were used to refine or determine structure. If no feedback from experimental data was used, this field is blank.

alumina films retain decreasing H contents as the growth temperature increases.[4,20−23] The hydrogen content is primarily from water rather than the methyl groups, as evidenced by isotopic studies.[22] Near the growth temperature used in this work (200 °C), films have been shown to retain 3−4 at. % hydrogen and very little carbon.[20,22] Finally, the density of ALD alumina also varies over a considerable range (2.4−3.5 g·cm^{-3}), depending primarily on the growth temperature.[4,22,24]

Since many ALD alumina films are structurally amorphous, understanding the effect of the short- and medium-range order on properties is critical for applications. A significant body of literature exists on the structures of amorphous and molten aluminas, although very few studies have examined ALD alumina. Of most interest to the present work, various studies of X-ray,[25−30] electron,[31,32] and neutron[26,29,30,33] scattering of amorphous or molten alumina have been reported. These scattering data can be transformed into real-space to provide pair distribution functions (PDF) with information about short- and medium-range order (i.e., across length scales of 1−20 Å). These data can then be used to refine molecular dynamics (MD) or reverse Monte Carlo (RMC) simulations of atomic positions, yielding various structural quantities such as the average coordination number (e.g., $\overline{CN}_{Al}$ for the average coordination number around Al), the percentage of individual coordination numbers for each element (e.g., $^{[4]}$Al, for the percentage of Al coordinated by four oxygen atoms), bond angle distributions, and the presence of certain medium-range structures, such as assemblies of polyhedra.[26,34−36] Notably, in a study of molten alumina, Skinner et al., used neutron and X-ray scattering and PDF data on molten alumina in combination with RMC simulations to quantify a predominance of $^{[4]}$Al (57.5%) and $^{[5]}$Al (34.7%) coordination numbers for Al with minority components of $^{[3]}$Al (3.5%) and $^{[6]}$Al (4.3%). These values for molten alumina are similar to other molten data and solid-state amorphous alumina and are presented in Table 1 for comparison to the present work. This similarity between molten and solid-state amorphous alumina is not surprising, as MD simulations show that the $\overline{CN}_{Al}$ of supercooled liquid alumina approached values measured for solid-state amorphous alumina samples.[30]

The local structure of solid state amorphous alumina has been primarily examined by solid-state NMR and scattering studies often coupled with atomistic simulations. Some variance has been observed in both the estimated average and distribution of coordination numbers (Table 1). Focusing on ALD films, NMR studies of plasma-enhanced ALD (PEALD) aluminum oxide revealed $^{[4]}$Al (54.3%), $^{[5]}$Al (40.6%), $^{[6]}$Al (5.1%). Quantification of coordination numbers in NMR involves the integration of distinct NMR peaks, as opposed to MD/RMC methods that rely on a cutoff pair distance to define which pairs are "bonded". Thus, agreement between these two methods at determining the coordination number may not occur. X-ray scattering and PDF analysis coupled with RMC simulations on ALD alumina−carbon nanotube composites was recently reported.[25] This work showed a similar PDF profile to molten alumina, and RMC analysis indicated an average coordination number for Al of $\overline{CN}_{Al}$ = 4.76. Similar information, albeit with a higher $\overline{CN}_{Al}$ was found for cryoelectron-based scattering and PDF analysis.[31] Importantly, this prior work on electron and X-ray PDFs of ALD alumina exploited the high surface area of carbon nanotubes as a growth substrate, which may result in a different local or long-range structure compared to most ALD thin films due to the high degree of curvature.[37]

An understanding of ALD alumina thin films and, in general, how synthetic factors lead to observed changes in measured properties, such as electronic defects, has proven difficult for amorphous materials. Accurate first principle calculations, such as density functional theory (DFT), that have proven useful in understanding the properties of crystalline materials are hindered by N^3 scaling (N being a measure of system size, i.e., atoms, bands or basis functions, and unit cell volume), and amorphous materials typically need large unit cells (on the order of thousands to tens of thousands of atoms) to accurately match experimental PDFs. Further, imposing any periodicity on an aperiodic system will inherently create artifacts that may only be due to the model and not the material. Thus, first-principles predictions for amorphous materials have been limited to those for which relatively small unit cells (<500 atoms) are generated directly by MD[38] or at the local density approximation[39] level of theory.

The cited investigations of ALD alumina have yielded deep insight and understanding of their compositions and how the composition is affected by deposition temperature, chemistry, and postprocessing. However, little is known about the local structure in ALD alumina, and X-ray PDF data on planar ALD alumina has not yet been reported. Further, the structural evolution by post-deposition heating presents some valuable scientific questions. For instance, is there an evolution in the medium-range order prior to crystallization? In addition, without a good experimental understanding of the local atomic structure of ALD alumina, it is difficult to build accurate computational models that might yield a better understanding

https://doi.org/10.1021/acsomega.2c04402
ACS Omega 2022, 7, 41033−41043

of the what structural motifs that lead to the measured properties, such as fixed charge,[40,41] of these important films.

Here, we combine grazing incidence synchrotron X-ray scattering, MD simulations, and DFT-based calculations to provide a better understanding of the geometric and electronic structures of amorphous ALD films. In particular, grazing incidence synchrotron X-ray scattering data were compared to MD simulations that modeled short- and medium-range order in amorphous ALD alumina planar thin films in the as-deposited state and after annealing at 450 and 700 °C in air. MD-generated unit cells exhibiting similar the short- and medium-range characteristics of the ALD films were analyzed using DFT, providing evidence of possible structural motifs that lead to the trap states in these films.

EXPERIMENTAL

Film Growth. Borosilicate glass substrates (Corning 1737 AMLCD, 25 × 75 mm) were cleaned via sonication for 5 min and subsequently by the Radio Corporation of America-1 (RCA-1) process. ALD was performed at 200 °C using TMA and water, which were both held at room temperature. Approximately 1.7−1.9 μm films were grown using a Veeco-CNT Savannah 200 ALD system. ALD pulse times were 0.015 s for TMA and water, and a purge time of 8 s was used between pulses, resulting in a growth rate of ∼1 Å/cycle. The samples were then coated halfway with a photoresist. To provide a known fluorescent material for footprint calibrations, the samples were then coated with approximately 10 nm of hafnium oxide by ALD using tetrakis(dimethylamido)hafnium-(IV) (TDMAH) and water at a substrate temperature of 120 °C. The photoresist was then removed via 5 min of sonication in acetone and subsequent rinsing with acetone, isopropyl alcohol, and water. The samples underwent post-deposition anneals of 450 and 700 °C under a continuous flow of nitrogen, and one sample was left in the as-deposited state. Spectator wafers without the hafnia coating were also processed in parallel as control samples.

Film Measurements. Grazing incidence total X-ray scattering[44] measurements were then carried out on the thin films at beamline 10−2 of the Stanford Synchrotron Radiation Lightsource (SSRL) using a 21.5 keV monochromatic focused X-ray beam narrowed using a pair of roller slits to dimensions of ∼30 μm × 50 μm. In order to measure the high-Q total scattering, the beamline consisted of soller slits and a silicon drift detector (Vortex). A full multichannel analyzer (MCA) spectrum was collected at every scattering point and utilized to extract elastic, inelastic or Compton, and fluorescence signals via spectrum analysis. Following careful alignment, X-ray reflectivity (XRR) data and Hf L-edge fluorescence signals (L_α, L_β, and L_γ) from the hafnium oxide capping layer were collected as a function of incidence angle for each sample. Based on these XRR data and angle curves, the critical angle was determined, and an appropriate incident angle (ca. 0.14 deg.) was selected to maximize scattering from the ALD Al_2O_3 film. This fluorescence optimization was coupled with scattering scans as a function of the incident angle to ensure the X-ray beam was fully attenuated before reaching the borosilicate glass substrate. Total scattering data were collected from momentum transfer (Q) from 0.1 to 20.1 Å^{-1}, with a Q-weighted counting scheme to ensure the data were of a statistically significant quality up to 20 Å^{-1}. This upper limit in the Q range is due to constraints on the grazing incidence setup for such thin films. Typically, a counting scheme was used to ensure at least 10 000 counts at each Q value to ensure a noise level of 1% or better based on Poisson statistics; typically, at least three scans were averaged for each sample before data analysis. An air scatter scan was also collected as a correction for low-Q data.

To probe the sample composition, RBS data were collected at Rutgers University using a General Ionex Tandetron with a beam of 2.0 MeV He^{2+} ions. A solid-state detector was placed at a backscatter angle of 163°. The combined beam and detector resolution was 21 keV. Data were fit using SimNRA. X-ray photoelectron spectroscopy (XPS) data were collected using a Thermo K-Alpha system. Electrons were excited using a monochromated Al Kα source with an energy of 1486.7 eV. The total instrumental resolution was 0.5 eV. Films were measured in the as-received state and after Ar sputter etching intended to remove approximately 10 nm of material. Elemental compositions were estimated by subtracting a Shirley background from the Al, O, and C spectra and normalizing each peak area by its Scofield cross section and the inelastic mean free path calculated using the Tanuma−Powell−Penn approximation.

PDFgui simulations. Computer-generated $G(r)$ data from crystal files were created using PDFgui.[45] Crystallographic information files were loaded, and $G(r)$ data were generated with the following parameters: ADP = 0.003, Q_{damp} = 0.001, Q_{broad} = 0, and Q_{max} = 18.1. The θ-Al_2O_3 structure was also fit in PDFgui (denoted θ_{fit}) to the experimental $G(r)$ data, in which case the cell parameters (a, b, and c), ADP, the scale factor, and Q_{damp} were adjusted to attempt to match the experimental data.

Molecular Dynamics. Classical molecular dynamics (MD) techniques were utilized to simulate amorphous alumina. The interatomic pair potentials describing the system energy and the force on each atom as a function of the atomic configuration are a combination of a long-range Coulombic interaction and a short-range Buckingham potential, leading to the following form for the potential energy between a pair of atoms:

$$V(r) = \frac{Z_\alpha Z_\beta e^2}{r} + A_{\alpha\beta}\exp\left(\frac{-r}{B_{\alpha\beta}}\right) - \frac{C_{\alpha\beta}}{r^6}$$

where r is the distance between atoms α and β and Z is the effective charge of an atom (in units of electron charge e). In simulations here, the long-range Coulombic contribution was computed using an Ewald summation approach with a real-space calculation cutoff of 12 Å; short-range Buckingham contributions were also cut off at 12 Å. The pair specific parameters A, B, and C and partial charge values Z for the Al_2O_3 system were originally advanced by Matsui.[46] This potential was subsequently shown to predict many properties of the Al_2O_3 system in agreement with the experiment, including crystalline structures, density, bulk moduli, thermal expansion behavior, and melting point.[47,48] This potential was also used to explore both the liquid state and the quenched amorphous structure and demonstrated agreement with experimental results, particularly for pair separation distances.[36,49] In all simulations, a time step of Δt = 0.0005 ps was used; this time step ensured numerical stability in high-temperature simulations. The open-source simulation code LAMMPS was used for all MD simulations.[50] The simulated amorphous samples were generated using a melt−quench procedure.

https://doi.org/10.1021/acsomega.2c04402
ACS Omega 2022, 7, 41033−41043

Samples with N = 5760 atoms (1152 Al_2O_3 stoichiometric units) were initially constructed in an α-Al_2O_3 structure and then melted at T = 5000 K in an isothermal−isobaric ensemble (NPT with P = 1 atm) for a simulation duration of 100 ps. Following this, maintaining an isobaric P = 1 atm condition, the temperature was reduced to T = 2400 K over a simulation duration of 100 ps. During a subsequent NPT ensemble simulation at T = 2400 K, diffusion analysis again ensured the system was in a liquid phase; the density at this state point was ρ = 2.83 g/cc. Next, maintaining P = 1 atm, simulated systems were quenched to T = 300 K over a prescribed time duration corresponding to a specified quench rate. Quench rates (dT/dt) explored here varied from 1×10^{11} to 1×10^{14} K/s. After the system was quenched to T = 300 K, a 100 ps simulation in an NPT ensemble was run with T = 300 K; the last 50 ps of that simulation was used to compute structural data. Simulations were demonstrated to be free from system size effects by the negligible difference in the thermodynamic behavior during the quench (e.g., density versus T) and the structural characterization at T = 300 K (e.g., radial distribution function analysis) between systems with N = 5760 atoms and N = 57600 atoms.

MD simulations were also used to generate smaller amorphous Al_2O_3 structures with N = 240 atoms (58 stoichiometric units). Such small systems, while amenable to density functional theory (DFT) calculations, truncate atomic interactions at a distance less than the classical interatomic potential cutoff, resulting in glass transformation temperatures higher than those observed for simulated system sizes that fully saturated the interatomic potential (i.e., N = 5760 atoms). Thus, for the N = 240 atom systems, the quench to T = 300 K was started from the equilibrated melt simulation at T = 5000 K and quenched with $dT/dt = 1.5 \times 10^{13}$ K/s. Because N = 240 atom systems exhibit a limited number of structural motifs, five different samples were prepared to account for structural variation. The five samples were obtained by beginning the quench to T = 300 K at different points in time during the preceding melt simulation at T = 5000 K.

DFT. First-principles calculations were carried out using density functional theory (DFT) and the electron projector-augmented wave (PAW) scheme as implemented in the Vienna Ab Initio Simulation Package (VASP).[51,52] Each calculation was performed using a 400 eV plane-wave cutoff coupled with the hybrid HSE06[53] correlation-exchange functional and the following [core]valence configurations for each element: Al = [Ne]3s3p and O = [He]2s2p. Density of states (DoS) calculations for the crystalline α- and θ- and θ_{Fit}-Al_2O_3 polymorphs were accomplished using 30 and 10 atom unit cells, respectively, with k-space integrations over an 8 × 8 × 12 Γ-centered k-point grid. As the amorphous unit cells are not definable by k-vectors, we report only the DoS sampled at the Γ-point (i.e., the 1 × 1 × 1 grid). Because of the large lattice dimensions of the N = 240 unit cells, the Γ-point-sampled electronic structure likely captures a large number of the electronic states of each unit cell.

RESULTS AND DISCUSSION

X-ray Scattering Data and Comparison to Crystalline Polymorphs. The alumina samples were all deposited at a sample temperature of 200 °C and split such that some samples were annealed at temperatures of either 450 or 700 °C to investigate potential thermally induced changes in short- and medium-range orders. RBS and XPS performed on these samples indicated that, as expected, the O/Al ratio was 1.5 ± 0.1. Additionally, the carbon content after ∼10 nm of Ar^+ sputtering was less than 1%, matching what has generally been observed using these growth conditions.[54]

Elastic X-ray scattering measurements (21.5 keV) were conducted on ALD alumina thin films in a grazing incidence geometry.[44] $I(Q)$ data were corrected for air-scattering, absorption, Lorentz effects, polarization effects, Compton scattering, and geometric dependency on momentum transfer and then normalized to determine the X-ray-weighted total structure factor, $S(Q)$, using PDFgetX2[55] (Figure 1). The $S(Q)$ data show broad features and peak locations similar to the measured $S(Q)$ of molten alumina and ALD alumina on

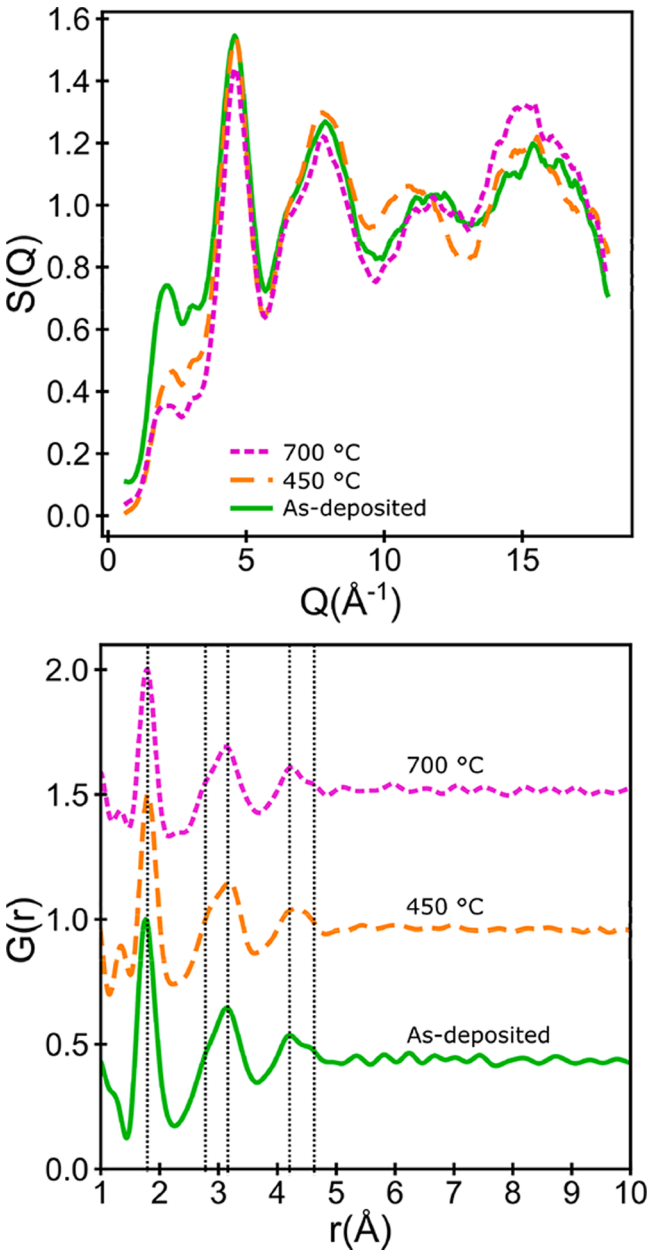

Figure 1. (top) Smoothed $S(Q)$ data and (bottom) corresponding $G(r)$ data for the as-deposited sample and the samples annealed at 450 and 700 °C. Vertical lines indicate approximate peak positions in experimental $G(r)$.

https://doi.org/10.1021/acsomega.2c04402
ACS Omega 2022, 7, 41033−41043

carbon nanotube supports,[25,30] providing evidence of the similarity in the short-range structure.

The $S(Q)$ was smoothly damped to zero at the high Q range using a Lorch function[56] to mitigate finite inverse Fourier transform artifacts. These data were then transformed into real space $G(r)$ data (Figure 1, pair distances where clear peaks were observed are marked with vertical dashed lines). Beyond 5 Å, no features were observed in the $G(r)$ data . No significant differences in the $G(r)$ data were observed among the three ALD alumina samples with different thermal histories, providing evidence that no major structural changes occurred after annealing at temperatures up to 700 °C, the highest temperature accessible for this experiment due to the stability of the borosilicate glass substrates. Specifically, no evidence for the emergence of medium- or long-range order was found. While 700 °C is below the temperature where crystallization (emergence of long-range order) has been observed in prior studies,[14−19] this result provides evidence that no changes in the medium- or short-range order occur at these intermediate temperatures.

The experimental ALD alumina $G(r)$ data were compared with $G(r)$ data of several known aluminum oxide and hydroxide phases to search for similarity in the short-range order (Figure 2). The first peak, which is associated with Al−O pair separation (1.76 Å, reported from the peak center), is notably shorter in the experimental data than those for most of the crystalline phases, including the thermodynamically stable α-alumina (1.94 Å), with the exception of κ- and θ-alumina (1.87 and 1.79 Å, respectively); θ-alumina shows the closest match. A decrease in the nearest-neighbor coordination relative to crystalline polymorphs was previously measured in molten metal oxides and may play some role in this short bond length relative to the known crystalline polymorphs.[57] The second and third peaks of both the κ and θ phases align closely with those of experimental ALD alumina $G(r)$. The comparison to θ-alumina, which has both four and six-coordinate Al species, has been invoked in prior ALD alumina X-ray scattering studies.[25] The appropriateness of this structural analog is evidenced by considering the average $\overline{CN}_{Al}$ of 5 in the θ phase and the fact that prior studies of molten and amorphous aluminas have generally shown $\overline{CN}_{Al}$ values ranging from approximately 4.2 to 4.9 (Table 1). Thus, these data provide further confirmation that planar ALD alumina may exhibit similar *average* short-range order (SRO) compared to molten alumina, θ-alumina, and ALD alumina deposited on carbon nanotubes.[25]

To further investigate potential SRO matches to θ-alumina, the crystalline polymorph was modified and fit to the experimental data using PDFgui (Figure 3).[45] Although

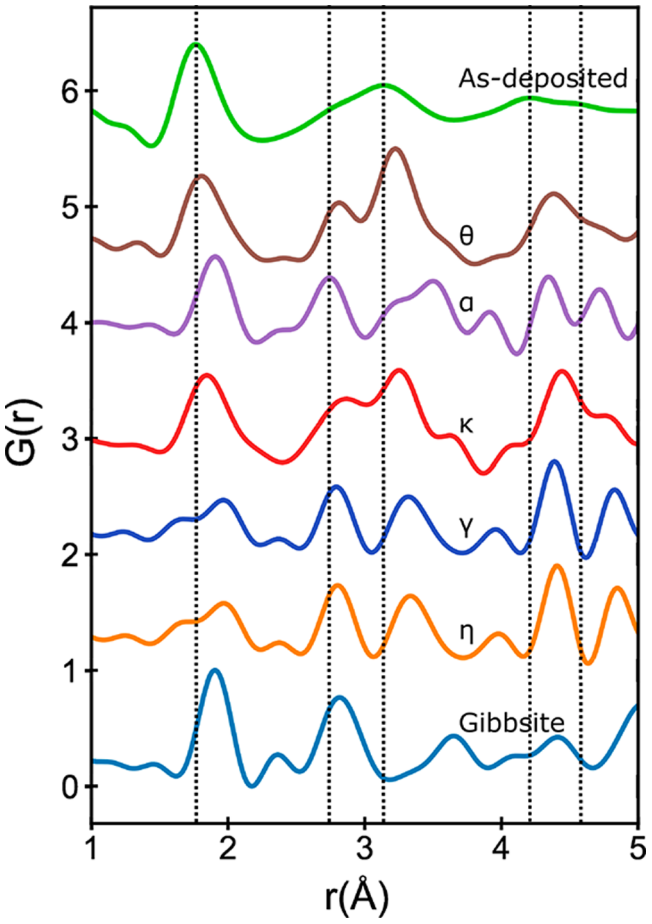

Figure 2. From top to bottom: experimental $G(r)$ data for as-deposited ALD alumina and simulated $G(r)$ data for selected Al_2O_3 phases and Gibbsite ($Al(OH)_3$). Note that γ- and η-phases show identical $G(r)$ data, as they are the same structure. Vertical lines are drawn at approximate peak positions for the experimental data, as described in Figure 1b.

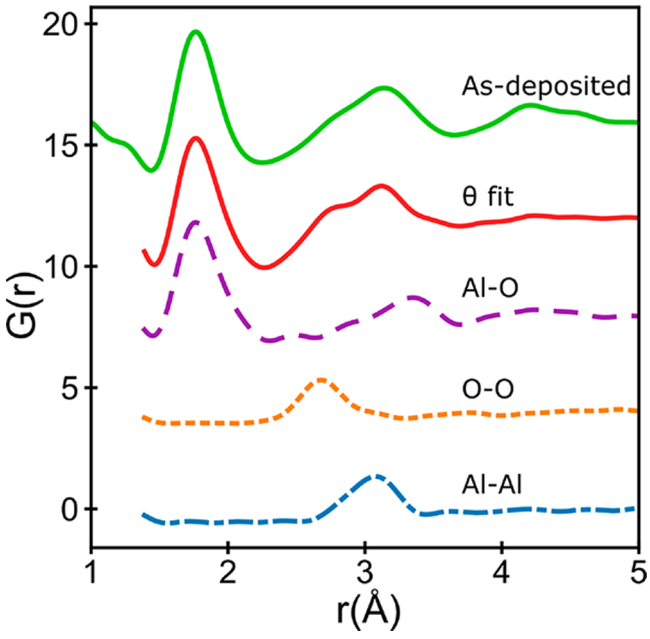

Figure 3. From top to bottom: experimental $G(r)$ data for as-deposited ALD alumina and θ-Al_2O_3 fit to experimental data using PDFgui and partial $G(r)$ data for Al−O, O−O, and Al−Al pairs from the θ-Al_2O_3 fit.

PDFgui models the X-ray PDF of a crystal, the unit cell parameters, atomic displacement parameters, and broadening parameters can all be modified to fit the experimental PDF and may provide a simple model for the SRO in amorphous ALD alumina and an assignment of features in $G(r)$ to specific atomic pairs. Parameters that were modified to fit the experimental data are shown in the Supporting Information (Table S1). The θ-Al_2O_3 $G(r)$ data, a fit to the experimental data (θ_{fit}), and the partial $G(r)$ data for each pair are shown along with the experimental $G(r)$ data in Figure 3. The

https://doi.org/10.1021/acsomega.2c04402
ACS Omega 2022, 7, 41033−41043

experimental $G(r)$ data match well with the PDFgui-simulated $G(r)$ data, with differences primarily in the relative intensities of peaks rather than peak locations. Notably, the first peak corresponding to the Al−O pair is shifted in the θ_{fit} from 1.79 to 1.77 Å. Peak positions in the partial $G(r)$ plot for O−O and Al−Al pairs were observed beginning near 2.6 and 3.0 Å, corresponding to the second and third features in the experimental data, respectively. From this simple simulated model, one can provide possible primary structural units (PSUs) for this amorphous structure based on $^{[4]}$Al and $^{[6]}$Al consisting of corner-sharing tetrahedra and corner- and edge-sharing octahedra, respectively. Although these PSUs are certainly an oversimplification of the structural diversity within the actual films, they give a representative molecular understanding of the film. One obvious shortfall of this simple model is the lack of fivefold-coordinated Al species, which have been observed in amorphous or molten samples both experimentally and in simulations.[26,30,36,42,43]

Molecular Dynamics Modeling. In order to move beyond structural modeling based on known alumina polymorphs to a physics-informed "bottom up" approach, classical MD simulations were used to generate amorphous Al_2O_3 atomic configurations for comparison to the experiment. Experimental systems studied here were prepared via ALD, but the atomic-scale modeling of ALD at experimental growth rates is not yet possible due to time constraints on MD simulations. Thus, simulated amorphous samples were generated using a melt−quench procedure. Because sample preparation methods differ between the simulation and the experiment, it is important to justify comparing results from one to the other. Most notably, prior simulation studies that explored the liquid and amorphous Al_2O_3 state using the same potential model used here demonstrated agreement with experiment, particularly for pair separation distances. In prior work examining the amorphous state, a melt−quench procedure was used while experimental data came from samples prepared via the anodic oxidation of aluminum foils. Thus, the model used here should predict an amorphous structure with pair separation distances in agreement with the experiment despite the fact that the computational work described here does not model the ALD growth process.

The true nature of the amorphous structure is well represented by the N = 5760 atom systems, which are large enough to accurately capture the thermodynamics and kinetics inherent in the underlying material model (i.e., the interatomic potential functions). Quench rates spanning three orders of magnitude were used to prepare simulated amorphous samples, resulting in negligible differences in simulated densities. For example, the equilibrated T = 300 K density was ρ = 3.23 g/cm^3 for the fastest quench rate $dT/dt = 1\times 10^{11}$ K/s, while ρ = 3.23 g/cm^3 for the for the slowest quench rate $dT/dt = 1\times 10^{11}$ K/s. Since the error in those values is on the order of 1%, the difference observed is not statistically significant. Note that the density values obtained were in the upper half of the somewhat broad range of density that has been observed experimentally for amorphous Al_2O_3 samples (2.4−3.5 g/cm^3).[4,22,24,58]

Minimal differences existed between simulated $G(r)$ data (Figure 4) for all quench rates using N = 5760 atom systems quenched to T = 300 K; for discussion here, data from one representative run are shown. $G(r)$ bin atomic separation distances were simulated without accounting for species-dependent scattering and other effects that influence peak

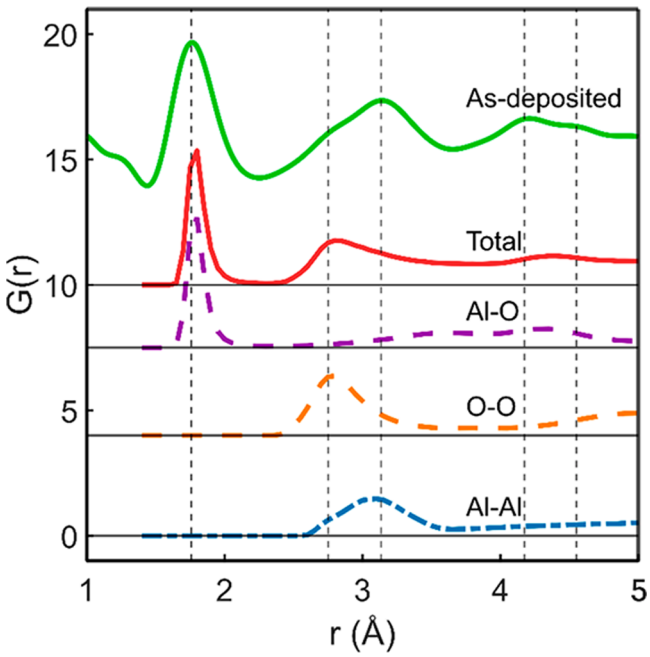

Figure 4. From top to bottom: experimental X-ray $G(r)$ data from the as-deposited ALD sample, total $G(r)$ from the MD simulation, and partial $G(r)$ data for the Al−O, O−O, and Al−Al pairs.

intensities in experimental PDF data. Since peak positions are unaltered by such effects, instead of comparing $G(r)$ data from the experiment and the simulation directly, we compare peak positions obtained from simulated partial $G(r)$ data (Figure 4) to peak positions observed in the experimental $G(r)$ plot . The position of the first neighbor peak in simulated Al−O partial $G(r)$ data (1.8 Å) agrees well with the first peak position observed in the experimental $G(r)$ plot. Simulated Al−Al partial $G(r)$ data exhibit a broad first peak whose position (3.1 Å) is also in good agreement with a peak observed in the experimental $G(r)$ plot. Data from the simulated O−O partial $G(r)$ plot exhibit a first peak at 2.8 Å; at the same separation distance, a shoulder feature is present on the broad second peak in the experimental $G(r)$ plot. Lastly, a relatively small peak exists in simulated Al−O partial $G(r)$ data at 4.3 Å, which is in agreement with a peak observed in the experimental $G(r)$ plot. These observations provide evidence that the amorphous Al_2O_3 structure obtained from MD simulations is comprised of short- to medium-range bonding environments similar to those that exist in the ALD-deposited samples. However, we note that the MD-derived models may not capture all of the bonding motifs in the actual ALD alumina samples. Given this, simulated atomic ensembles were used to characterize the short- and medium-range bonding environments in greater detail.

Simulated atomic configurations can be used to characterize bonding environments with greater detail than can be obtained from experiments.[59−62] The average coordination number of O atoms around Al as a function of the cutoff distance R_c (Figure 5a) and the average coordination numbers (averaged over time and all Al atoms in the system, Table 1) match well with previous studies, which used coordination cutoffs (R_c) between 2.2 ($\overline{CN}_{Al}$ = 4.24) and 2.5 Å ($\overline{CN}_{Al}$ = 4.41). Examining coordination statistics for both of these cutoff distances shows that the coordination is dominated by fourfold-coordinated Al and threefold-coordinated O. In addition, the bond angle

https://doi.org/10.1021/acsomega.2c04402
ACS Omega 2022, 7, 41033−41043

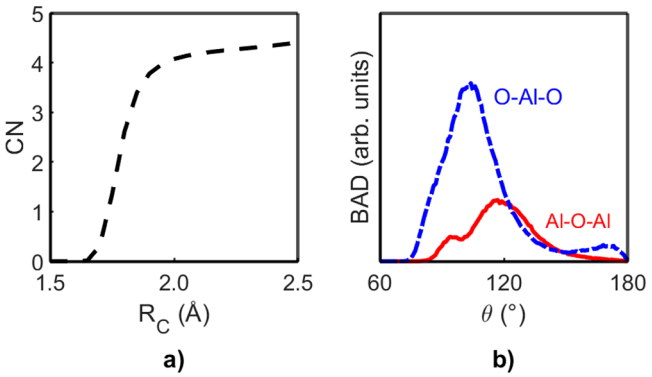

Figure 5. Results for simulated amorphous Al_2O_3 using N = 5760 atoms. (a) Average coordination number (CN) of O around Al as a function of the cutoff distance R_c used to find atoms within the first coordination sphere. (b) Bond angle distributions for Al−O−Al (solid, red) and O−Al−O (dashed, blue).

distributions (BADs, Figure 5b) for the O−Al−O and Al−O−Al triplets were computed (R_c = 2.2 Å). The primary peak near 104° in the O−Al−O bond angle distribution results from tetrahedrally coordinated Al atoms, and the small secondary peak near 170° results from fivefold-coordinated Al atoms. For the Al−O−Al bond angle distribution, the peaks near 95° and 120° correspond generally to edge- and corner-sharing polyhedra, respectively, as observed in prior work.[26,34,36,63]

In addition to characterizing atomic bonding environments, classical MD simulations were used to prepare amorphous Al_2O_3 atomic ensembles for the DFT calculation of the electronic structure; five N = 240 atom systems were generated. Each system started the quench procedure from a different starting state in the preceding T = 5000 K melt simulation. The average approximate edge length for the N = 240 simulation cells is 13.5 Å, which ensure that atomic interactions out to second and third neighbor shells are well represented. Density, $G(r)$, and BADs for these five systems were compared to results for the N = 5760 atom system. Although an identical quench rate was used in each of the N = 240 simulation procedures, variation existed in their T = 300 K quenched density, which spanned from ρ = 3.05 g/cm^3 to ρ = 3.30 g/cm^3. For comparison to the N = 5760 atom system, after quenching and equilibration at T = 300 K, all N = 240 atom systems were scaled in atomic space to have the same density as the N = 5760 atom system (ρ = 3.244 g/cm^3). Scaled systems were then re-equilibrated for a 100 ps duration. Density scaling resulted in the observation of at most a 2% change in peak positions in full and partial $G(r)$ data and did not affect the overall shape of any structural distribution presented here. The largest observed changes in coordination statistics due to scaling were comparable to the approximate error in those calculations (i.e., approximately 1−2%). Thus, all comparison data presented here are for constant-density atomic ensembles.

For each of the partial $G(r)$ plots, significant variation among the five N = 240 atom systems is evident (Figure 6). Since $G(r)$ is a histogram of atom pair distances, smaller system sizes result in selective population of the histogram and lead to variation among samples. Nonetheless, the pair separation distances in the N = 240 atom systems are consistent with those in the N = 5760 atom system, as evidenced by the similarity between the average curve for the

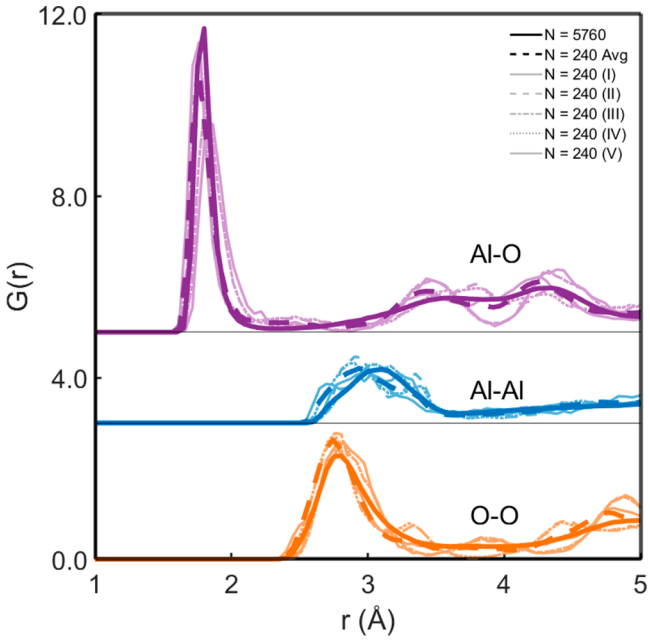

Figure 6. Partial $G(r)$ for simulated amorphous Al_2O_3 systems. Three sets of seven curves are shown; from top to bottom, they are for the Al−O, Al−Al, and O−O pairs. For each set of curves, five are presented with lower line weights; those five curves each represent data from each of the five N = 240 atom systems. Two curves in each set are shown in heavier line weights; one is an average over the data from five N = 240 atom systems (dashed), and one is for the N = 5760 atom system (solid).

N = 240 atom systems and the N = 5760 atom system (Figure 6).

Table 2 presents Al−O coordination statistics for the MD models. The differences in coordination statistics in the N = 240 atom systems correlate with variations in partial $G(r)$ data in Figure 6. For example, samples III and V exhibit characteristic increases in the concentration of fivefold- and sixfold-coordinated Al along with an increased concentration of fourfold-coordinated O. Those same two systems are the ones whose first Al−O peaks in Figure 6a are shifted to slightly larger separation distances, and Al−O bond lengths for fivefold- and sixfold-coordinated Al atoms are, on average, somewhat larger than those for fourfold-coordinated Al atoms.

Table 2. Coordination Statistics in Amorphous Al_2O_3 Models Here[a]

system	$^{[2]}$O	$^{[3]}$O	$^{[4]}$O	$^{[5]}$O	$^{[3]}$Al	$^{[4]}$Al	$^{[5]}$Al	$^{[6]}$Al
N = 5760	19.3	78.5	2.2	0	0.1	77.0	21.3	1.6
N = 240 (avg)	18.7	71.1	9.9	0.3	1.1	65.3	28.2	5.3
N = 240 (I)	22.1	68.7	9.2	0	1.0	71.2	23.8	4.0
N = 240 (II)	24.5	70.9	4.5	0	1.2	79.5	17.3	2.0
N = 240 (III)	15.2	72.7	11.8	0.3	0	60.9	32.3	6.8
N = 240 (IV)	23.7	67.6	8.7	0	3.3	69.4	24.1	3.2
N = 240 (V)	8.1	75.4	15.2	1.3	0.2	45.5	43.8	10.5

[a]Values are percentages obtained using R_c = 2.2 Å, where $^{[n]}$A is n-fold coordinated A (atom).

https://doi.org/10.1021/acsomega.2c04402
ACS Omega 2022, 7, 41033−41043

This is similar to some crystalline polymorphs that exhibit sixfold-coordinated Al; for those species, Al−O bond lengths are longer. For example, this longer Al−O bond length can be observed in Figure 2 for gibbsite ($Al(OH)_3$) and α-Al_2O_3. Coordination data in Table 2 for N = 240 atom systems, particularly on average, agree with data for the N = 5760 atom system.

While it might appear that there are larger differences between the N = 240 and N = 5760 atom systems for BADs than for partial $G(r)$, this is a statistical effect. Specifically, data in $G(r)$ are based on atomic pairs, while data in BADs are based on atomic triplets, making the variation in BADs for small systems more significant. Qualitatively, BADs (Figure 7)

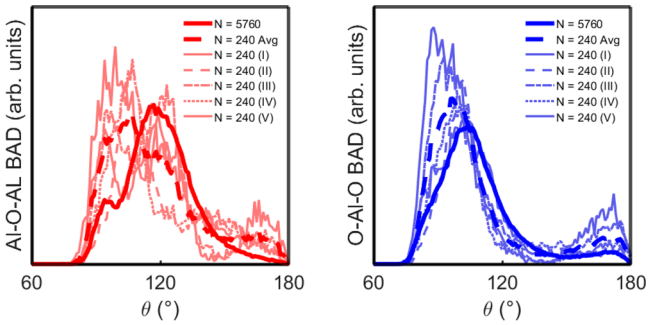

Figure 7. Bond angle distributions for (a) Al−O−Al and (b) O−Al−O in the simulated amorphous Al_2O_3 systems. There are seven curves in each plot, five of which are presented with lower line weights; those five curves each represent data from one of the five N = 240 atom systems. Two curves are shown in heavier line weights; one is an average of the data over the five N = 240 atom systems (dashed), and one is for the N = 5760 atom system (solid).

from the small systems agree with data from the large system in that the distributions all span effectively the same angle range, and there is some agreement in the overall distribution shape (number of peaks and peak position). The average plot of Al−O−Al bond angles (Figure 7a) for the N = 240 atom systems has two peaks whose positions are in reasonable agreement with the N = 5760 atom system, which generally correspond to corner- and edge-sharing polyhedra with reversed magnitudes. Some of the N = 240 atom systems show a small peak at high angles in both the Al−O−Al and O−Al−O bond angles that is not present in the data of the N = 5760 atom system. For the O−Al−O bond angle (Figure 7b), higher coordination Al atoms in some of the N = 240 atom systems push the first peak to a lower angle and increase the relative magnitude of the peak at the high angle.

Overall, our analysis suggests that these smaller systems are suitable as inputs for the DFT-based analysis of their electronic structure and for understanding how short- and medium-range order affect the electronic structure. Both the partial $G(r)$ data and BAD data for N = 240 atom systems show that the structural motifs present in those systems are properly representative of the N = 5760 atom system.

DFT Analysis of MD-Derived Amorphous Structure. The N = 240 atom cells created using MD were used as inputs in DFT calculations to examine the electronic structure of amorphous alumina. These are directly compared to that of crystalline (α and θ) Al_2O_3 and the PDFgui-modified θ_{fit} phase. The DoS of the crystalline Al_2O_3 structures confirms that in each crystalline polymorph the valence band (VB) is hybridized oxygen p and aluminum d orbitals while the conduction band (CB) is a mix of p and s character (Figure 8).[38,39,64] The largest band gap (E_G) is calculated for the α-

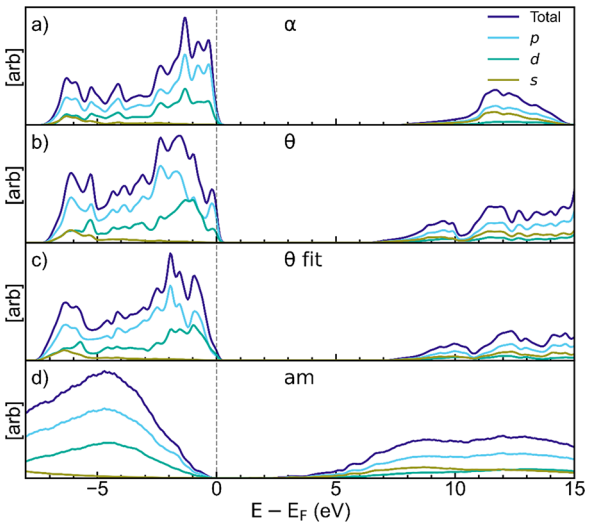

Figure 8. Projected density of states for (a−c) crystalline and (d) amorphous Al_2O_3 polymorphs. The amorphous density of states was obtained by averaging data across all five N = 240 samples (all are shown in Figure S2) and shows the characteristic disruption of the defined valence band and conduction band edges.

Al_2O_3 polymorph at 7.76 eV. This value was reduced to 6.46 and 7.08 eV for the θ and θ_{fit} polymorphs, respectively. The DoS values show that the increase in E_G from θ to θ_{fit} is due to the red-shifting of a small shoulder peak of mainly p character away from the Fermi energy (E_F) in θ_{fit}. This effect can be attributed shorter Al−O bond lengths and thus better orbital overlap between Al and O atoms, which result in a lower-energy peak in θ_{fit}. Similar differences in band edge positions arising from variations in the local Al−O symmetry were documented previously.[65]

The high disorder of amorphous Al_2O_3, the variation in the five N = 240 unit cells, and the symmetry restriction to Γ-point sampling could make the DFT analysis of the electronic structure of these materials difficult.[66−70] However, the slight variations seen in the $G(r)$ data and BADs of each N = 240 unit cell does not lead to a large difference in the DoS (Figure 8 and S2) or the orbital-resolved projected DoS (Figure S3). However, the atomic disorder creates a large number of tail states that result in the significant disruption of defined VB and CB edges, in comparison to the crystalline structures, and prevents the conclusive assignment of E_G. To gain further insight into the nature of these tail states, we calculated the inverse participation ratio (IPR) for each amorphous sample, which was defined for the ith Kohn−Sham orbital φ_i in real space as

$$\mathrm{IPR}(\varphi_i) = \frac{\sum_{i=1}^{N} |\varphi_i|^4}{\sum_{i=1}^{N} |\varphi_i^2|^2}$$

Such analysis has been used extensively to investigate the electronic properties of amorphous materials.[68,71,72] The IPRs for the five amorphous samples indicate that the greatest degree of localization occurs for electrons at the top of the VB (Figure S4), as delocalized bands are not found until ∼2 eV

https://doi.org/10.1021/acsomega.2c04402
ACS Omega 2022, 7, 41033−41043

below E_F. Inspection of the charge density of these tail states across all five samples shows that electrons localize in 2p orbitals centered on twofold-coordinated bridging oxygens (Figure S4). These states are unique to the amorphous structure, as the crystalline polymorphs contain only threefold- and fourfold-coordinated oxygens.

Above E_F, low IPR values indicate the formation of extended Bloch states that allow the qualitative estimation of the mobility edge, giving an approximate E_G of 6−7 eV for the amorphous samples. However, in several of the samples studied, localized electron traps occur ∼2 eV or more below the extended CB edge. These states consist of regions of localized charge density within cavities formed by Al−O ring-like structures in the material (Figure S4). Electron trapping in such sites was previously suggested to be the source of a number of observed properties, particularly negative charging in amorphous Al_2O_3 films.[73] Among the five amorphous samples studied here, the degree of localization, energetics, and structural motifs that contribute such electron traps are highly variable; however, all samples indicate that both twofold-coordinated oxygen and Al−O rings are critical structures that exist in the amorphous material that change the electronic properties of the material.

CONCLUSIONS

X-ray scattering-derived structural data were acquired for ALD alumina films with different thermal histories. Notably, similar short-range order was found for these samples compared to molten and other amorphous alumina samples. The closest crystalline structural analog was found to be θ-alumina. More realistic structural models were created using MD, and these models matched well with peak positions from the X-ray-based PDF data and prior MD results. Careful downscaling of the MD model size resulted in DFT-tractable models largely consistent with larger models. The calculated electronic structure confirmed that most of the properties of amorphous alumina are similar to those of θ-alumina. However, Al−O alternating ring structures and twofold-coordinated oxygen lead to midgap electron traps and the modification of the valence band edge, respectively.

ASSOCIATED CONTENT

Supporting Information

The Supporting Information is available free of charge at https://pubs.acs.org/doi/10.1021/acsomega.2c04402.

Table of parameters for PDFgui simulations and total density of states for N = 240 atom samples (PDF)

AUTHOR INFORMATION

Corresponding Authors

Nicholas C. Strandwitz − *Materials Science and Engineering Department, Lehigh University, Bethlehem, Pennsylvania 18015, USA;* orcid.org/0000-0001-6159-9430; Email: nis212@lehigh.edu

Edmund B. Webb III − *Mechanical Engineering and Mechanics Department, Lehigh University, Bethlehem, Pennsylvania 18015, USA*; Email: ebw210@lehigh.edu

Lisa A. Fredin − *Chemistry Department, Lehigh University, Bethlehem, Pennsylvania 18015, USA*; Email: lafredin@lehigh.edu

Authors

Anthony Pugliese − *Materials Science and Engineering Department, Lehigh University, Bethlehem, Pennsylvania 18015, USA*

Badri Shyam − *Xerion Advanced Battery Corporation, Kettering, Ohio 45420, USA*

Gil M. Repa − *Chemistry Department, Lehigh University, Bethlehem, Pennsylvania 18015, USA*

Anh Hung Nguyen − *Mechanical Engineering and Mechanics Department, Lehigh University, Bethlehem, Pennsylvania 18015, USA;* orcid.org/0000-0002-1457-9100

Apurva Mehta − *SLAC National Accelerator Laboratory, Menlo Park, California 94025, USA;* orcid.org/0000-0003-0870-6932

Complete contact information is available at: https://pubs.acs.org/10.1021/acsomega.2c04402

Funding

The authors acknowledge funding from Lehigh University and from NSF award 1605129.

Notes

The authors declare no competing financial interest.

ACKNOWLEDGMENTS

The authors thank Ritwik Bhatia of Veeco CNT for the deposition of the alumium oxide films.

REFERENCES

(1) Hoex, B.; Heil, S. B. S.; Langereis, E.; van de Sanden, M. C. M.; Kessels, W. M. M. Ultralow Surface Recombination of C-Si Substrates Passivated by Plasma-Assisted Atomic Layer Deposited Al2O3. *Appl. Phys. Lett.* **2006**, *89* (4), 042112.

(2) Hezel, R.; Jaeger, K. Low-Temperature Surface Passivation of Silicon for Solar Cells. *J. Electrochem. Soc.* **1989**, *136* (2), 518.

(3) Carcia, P. F.; McLean, R. S.; Reilly, M. H.; Groner, M. D.; George, S. M. Ca Test of Al 2O 3 Gas Diffusion Barriers Grown by Atomic Layer Deposition on Polymers. *Appl. Phys. Lett.* **2006**, *89* (3), 031915.

(4) Groner, M. D.; Fabreguette, F. H.; Elam, J. W.; George, S. M. Low-Temperature Al2O3 Atomic Layer Deposition. *Chem. Mater.* **2004**, *16* (4), 639−645.

(5) Johnson, R. S.; Lucovsky, G.; Baumvol, I. Physical and Electrical Properties of Noncrystalline Al2O3 Prepared by Remote Plasma Enhanced Chemical Vapor Deposition. *J. Vac. Sci. Technol. A Vacuum, Surfaces, Film.* **2001**, *19* (4), 1353−1360.

(6) Gusev, E. P.; Copel, M.; Cartier, E.; Baumvol, I. J. R.; Krug, C.; Gribelyuk, M. A. High-Resolution Depth Profiling in Ultrathin Al2O3 Films on Si. *Appl. Phys. Lett.* **2000**, *76* (2), 176−178.

(7) Puurunen, R. L. Surface Chemistry of Atomic Layer Deposition: A Case Study for the Trimethylaluminum/Water Process. *J. Appl. Phys.* **2005**, *97* (12), 121301.

(8) George, S. M. Atomic Layer Deposition: An Overview. *Chem. Rev.* **2010**, *110* (1), 111−131.

(9) Miikkulainen, V.; Leskelä, M.; Ritala, M.; Puurunen, R. L. Crystallinity of Inorganic Films Grown by Atomic Layer Deposition: Overview and General Trends. *J. Appl. Phys.* **2013**, *113* (2), 021301.

(10) Katz, M. B.; Twigg, M. E.; Prokes, S. M. Formation and Stability of Crystalline and Amorphous Al2O3 Layers Deposited on Ga2O3 Nanowires by Atomic Layer Epitaxy. *J. Appl. Phys.* **2016**, *120* (12), 124311.

(11) Prokes, S. M.; Katz, M. B.; Twigg, M. E. Growth of Crystalline Al2O3 via Thermal Atomic Layer Deposition: Nanomaterial Phase Stabilization. *APL Mater.* **2014**, *2* (3), 032105.

(12) Ngo, T. Q.; Goble, N. J.; Posadas, A.; Kormondy, K. J.; Lu, S.; McDaniel, M. D.; Jordan-Sweet, J.; Smith, D. J.; Gao, X. P. A.; Demkov, A. A.; et al. Quasi-Two-Dimensional Electron Gas at the

Interface of γ-Al2O3/SrTiO3 Heterostructures Grown by Atomic Layer Deposition. *J. Appl. Phys.* **2015**, *118* (11), 115303.
(13) Aarik, L.; Mändar, H.; Ritslaid, P.; Tarre, A.; Kozlova, J.; Aarik, J. Low-Temperature Atomic Layer Deposition of α-Al 2 O 3 Thin Films. *Cryst. Growth Des.* **2021**, *21* (7), 4220−4229.
(14) Afanas'Ev, V. V.; Stesmans, A.; Mrstik, B. J.; Zhao, C. Impact of Annealing-Induced Compaction on Electronic Properties of Atomic-Layer-Deposited Al2O3. *Appl. Phys. Lett.* **2002**, *81* (9), 1678−1680.
(15) Zhao, C.; Cosnier, V.; Chen, P. J.; Richard, O.; Roebben, G.; Maes, J.; Van Elshocht, S.; Bender, H.; Young, E.; Van Der Biest, O.; et al. Thermal Stability of High k Layers. *Mater. Res. Soc. Symp. - Proc.* **2002**, *745*, 9−14.
(16) Jakschik, S.; Schroeder, U.; Hecht, T.; Gutsche, M.; Seidl, H.; Bartha, J. W. Crystallization Behavior of Thin ALD-Al2O3 Films. *Thin Solid Films* **2003**, *425* (1−2), 216−220.
(17) Huntz, A.-M.; Andrieux, M.; Vahlas, C.; Sovar, M.-M.; Samelor, D.; Gleizes, A. N. Phase Transformations of Metallorganic Chemical Vapor Deposition Processed Alumina Coatings Investigated by In Situ Deflection. *Journal of The Electrochemical Society.* **2007**, *154*, P63.
(18) Zhang, L.; Jiang, H. C.; Liu, C.; Dong, J. W.; Chow, P. Annealing of Al2O3 Thin Films Prepared by Atomic Layer Deposition. *J. Phys. D. Appl. Phys.* **2007**, *40* (12), 3707−3713.
(19) Hsain, Z.; Zeng, G.; Strandwitz, N. C.; Krick, B. A. Wear Behavior of Annealed Atomic Layer Deposited Alumina. *Wear* **2017**, *372-373*, 139−144.
(20) Dingemans, G.; van de Sanden, M. C. M.; Kessels, W. M. M. Influence of the Deposition Temperature on the C-Si Surface Passivation by Al[Sub 2]O[Sub 3] Films Synthesized by ALD and PECVD. *Electrochem. Solid-State Lett.* **2010**, *13* (3), H76.
(21) Gosset, L. G.; Damlencourt, J.-F.; Renault, O.; Rouchon, D.; Holliger, P.; Ermolieff, A.; Trimaille, I.; Ganem, J.-J.; Martin, F.; Séméria, M.-N. Interface and Material Characterization of Thin Al 2 O 3 Layers Deposited by ALD Using TMA/H 2 O. *J. Non. Cryst. Solids* **2002**, *303* (1), 17−23.
(22) Guerra-Nuñez, C.; Döbeli, M.; Michler, J.; Utke, I. Reaction and Growth Mechanisms in Al_2O_3 Deposited via Atomic Layer Deposition: Elucidating the Hydrogen Source. *Chem. Mater.* **2017**, *29* (20), 8690−8703.
(23) Ott, A. W.; Klaus, J. W.; Johnson, J. M.; George, S. M. Al3O3 Thin Film Growth on Si(100) Using Binary Reaction Sequence Chemistry. *Thin Solid Films* **1997**, *292* (1−2), 135−144.
(24) Dingemans, G.; Einsele, F.; Beyer, W.; Van De Sanden, M. C. M.; Kessels, W. M. M. Influence of Annealing and Al 2 O 3 Properties on the Hydrogen-Induced Passivation of the Si/SiO 2 Interface. *Cit. J. Appl. Phys.* **2012**, *111*, 093713.
(25) Young, M. J.; Bedford, N. M.; Yanguas-Gil, A.; Letourneau, S.; Coile, M.; Mandia, D. J.; Aoun, B.; Cavanagh, A. S.; George, S. M.; Elam, J. W. Probing the Atomic-Scale Structure of Amorphous Aluminum Oxide Grown by Atomic Layer Deposition. *ACS Appl. Mater. Interfaces* **2020**, *12* (20), 22804−22814.
(26) Shi, C.; Alderman, O. L. G. G.; Berman, D.; Du, J.; Neuefeind, J.; Tamalonis, A.; Weber, J. K. R. R.; You, J.; Benmore, C. J. The Structure of Amorphous and Deeply Supercooled Liquid Alumina. *Front. Mater.* **2019**, *6*, 38 DOI: 10.3389/fmats.2019.00038.
(27) Manaila, R.; Devenyi, A.; Candet, E. Structural Order in Amorphous Aluminas. *Thin Solid Films* **1984**, *116* (1−3), 289−299.
(28) Ansell, S.; Krishnan, S.; Weber, J. K. R.; Felten, J. J.; Nordine, P. C.; Beno, M. A.; Price, D. L.; Saboungi, M. L. Structure of Liquid Aluminum Oxide. *Phys. Rev. Lett.* **1997**, *78* (3), 464−466.
(29) Lamparter, P.; Kniep, R. Structure of Amorphous Al2O3. *Phys. B Condens. Matter* **1997**, *234−236*, 405−406.
(30) Skinner, L. B.; Barnes, A. C.; Salmon, P. S.; Hennet, L.; Fischer, H. E.; Benmore, C. J.; Kohara, S.; Weber, J. K. R.; Bytchkov, A.; Wilding, M. C.; et al. Joint Diffraction and Modeling Approach to the Structure of Liquid Alumina. *Phys. Rev. B - Condens. Matter Mater. Phys.* **2013**, *87* (2), 53−58.
(31) Jasim, A. M.; He, X.; Xing, Y.; White, T. A.; Young, M. J. Cryo-EPDF: Overcoming Electron Beam Damage to Study the Local Atomic Structure of Amorphous ALD Aluminum Oxide Thin Films within a TEM. *ACS Omega* **2021**, *6* (13), 8986−9000.
(32) Zeng, L.; Tran, D. T.; Tai, C. W.; Svensson, G.; Olsson, E. Atomic Structure and Oxygen Deficiency of the Ultrathin Aluminium Oxide Barrier in Al/AlOx/Al Josephson Junctions. *Sci. Rep.* **2016**, *6* (March), 1−8.
(33) Landron, C.; Hennet, L.; Jenkins, T. E.; Greaves, G. N.; Coutures, J. P.; Soper, A. K. Liquid Alumina: Detailed Atomic Coordination Determined from Neutron Diffraction Data Using Empirical Potential Structure Refinement. *Phys. Rev. Lett.* **2001**, *86* (21), 4839−4842.
(34) Le, V. V.; Nguyen, V. H.; Nguyen, V. H.; Pham, K. H. The Structure and Mechanical Properties in Amorphous Alumina under Pressure. *Comput. Mater. Sci.* **2013**, *79*, 110−117.
(35) Van Hoang, V. Molecular Dynamics Study on Structure and Properties of Liquid and Amorphous Al_2O_3. *Phys. Rev. B - Condens. Matter Mater. Phys.* **2004**, *70* (13), 134204.
(36) Gutiérrez, G.; Johansson, B. Molecular Dynamics Study of Structural Properties of Amorphous (Formula Presented). *Phys. Rev. B - Condens. Matter Mater. Phys.* **2002**, *65* (10), 1−9.
(37) Prokes, S. M.; Katz, M. B.; Twigg, M. E. Growth of Crystalline Al2O3 via Thermal Atomic Layer Deposition: Nanomaterial Phase Stabilization. *APL Mater.* **2014**, *2* (3), 032105.
(38) Dicks, O. A.; Shluger, A. L. Theoretical Modeling of Charge Trapping in Crystalline and Amorphous Al2O3. *J. Phys.: Condens. Matter* **2017**, *29* (31), 314005.
(39) Davis, S.; Gutiérrez, G. Structural, Elastic, Vibrational and Electronic Properties of Amorphous Al2O3 from Ab Initio Calculations. *J. Phys.: Condens. Matter* **2011**, *23* (49), 495401.
(40) Hoex, B.; Gielis, J. J. H.; van de Sanden, M. C. M.; Kessels, W. M. M. On the *c*-Si Surface Passivation Mechanism by the Negative-Charge- Dielectric Al_2O_3. *J. Appl. Phys.* **2008**, *104* (11), 113703.
(41) Aboaf, J. a.; Kerr, D. R.; Bassous, E. Charge in SiO2-Al2O3 Double Layers on Silicon. *J. Electrochem. Soc.* **1973**, *120* (8), 1103.
(42) Lee, S. K.; Lee, S. B.; Park, S. Y.; Yi, Y. S.; Ahn, C. W. Structure of Amorphous Aluminum Oxide. *Phys. Rev. Lett.* **2009**, *103*, 095501.
(43) Lee, S. K.; Park, S. Y.; Yi, Y. S.; Moon, J. Structure and Disorder in Amorphous Alumina Thin Films: Insights from High-Resolution Solid-State NMR. *J. Phys. Chem. C* **2010**, *114* (32), 13890−13894.
(44) Shyam, B.; Stone, K. H.; Bassiri, R.; Fejer, M. M.; Toney, M. F.; Mehta, A. Measurement and Modeling of Short and Medium Range Order in Amorphous Ta_2O_5 Thin Films. *Sci. Rep.* **2016**, *6*, 32170.
(45) Farrow, C. L.; Juhas, P.; Liu, J. W.; Bryndin, D.; Božin, E. S.; Bloch, J.; Proffen, T.; Billinge, S. J. L. PDFfit2 and PDFgui: Computer Programs for Studying Nanostructure in Crystals. *J. Phys.: Condens. Matter* **2007**, *19* (33), 335219.
(46) Matsui, M. A Transferable Interatomic Potential Model for Crystals and Melts in the System CaO-MgO-Al2O3-SiO2. *Mineral. Mag.* **1994**, *58A* (2), 571−572.
(47) Ahuja, R.; Belonoshko, A. B.; Johansson, B. Melting and Liquid Structure of Aluminum Oxide Using a Molecular-Dynamics Simulation. *Phys. Rev. E* **1998**, *57* (2), 1673.
(48) Belonoshko, A. B. Melting of Corundum Using Conventional and Two-Phase Molecular Dynamic Simulation Method. *Phys. Chem. Miner. 1998 252* **1998**, *25* (2), 138−141.
(49) Gutiérrez, G.; Belonoshko, A. B.; Ahuja, R.; Johansson, B. Structural Properties of LiquidAl2O3: A Molecular Dynamics Study. *Phys. Rev. E* **2000**, *61* (3), 2723.
(50) Plimpton, S. Fast Parallel Algorithms for Short-Range Molecular Dynamics. *J. Comput. Phys.* **1995**, *117* (1), 1−19.
(51) Blöchl, P. E. Projector Augmented-Wave Method. *Phys. Rev. B* **1994**, *50* (24), 17953−17979.
(52) Kresse, G.; Furthmuller, J. Efficient Iterative Schemes for Ab Initio Total-Energy Calculations Using a Plane-Wave Basis Set. *Phys. Lett. B* **1996**, *54* (16), 11169−11186.
(53) Heyd, J.; Scuseria, G. E.; Ernzerhof, M. Hybrid Functionals Based on a Screened Coulomb Potential. *J. Chem. Phys.* **2003**, *118* (18), 8207−8215.

https://doi.org/10.1021/acsomega.2c04402
ACS Omega 2022, 7, 41033−41043

(54) Groner, M. D.; Elam, J. W.; Fabreguette, F. H.; George, S. M. Electrical Characterization of Thin Al2O3 Films Grown by Atomic Layer Deposition on Silicon and Various Metal Substrates. *Thin Solid Films* **2002**, *413* (1−2), 186−197.
(55) Qiu, X.; Thompson, J. W.; Billinge, S. J. L. PDFgetX2: A GUI-Driven Program to Obtain the Pair Distribution Function from X-Ray Powder Diffraction Data. *J. Appl. Crystallogr.* **2004**, *37* (4), 678−678.
(56) Lorch, E. Neutron Diffraction by Germania, Silica and Radiation-Damaged Silica Glasses. *J. Phys. C Solid State Phys.* **1969**, *2* (2), 229.
(57) Skinner, L. B.; Benmore, C. J.; Weber, J. K. R.; Du, J.; Neuefeind, J.; Tumber, S. K.; Parise, J. B. Low Cation Coordination in Oxide Melts. *Phys. Rev. Lett.* **2014**, *112* (15), 157801.
(58) Gorham, C. S.; Gaskins, J. T.; Parsons, G. N.; Losego, M. D.; Hopkins, P. E. Density Dependence of the Room Temperature Thermal Conductivity of Atomic Layer Deposition-Grown Amorphous Alumina (Al2O3). *Appl. Phys. Lett.* **2014**, *104* (25), 253107.
(59) Sørensen, S. S.; Biscio, C. A. N.; Bauchy, M.; Fajstrup, L.; Smedskjaer, M. M. Revealing Hidden Medium-Range Order in Amorphous Materials Using Topological Data Analysis. *Sci. Adv.* **2020**, *6* (37), eabc2320 DOI: 10.1126/sciadv.abc2320.
(60) Tavanti, F.; Calzolari, A. Multi-Technique Approach to Unravel the (Dis)Order in Amorphous Materials. *ACS Omega* **2022**, *7*, 23255.
(61) Rieser, J. M.; Goodrich, C. P.; Liu, A. J.; Durian, D. J. Divergence of Voronoi Cell Anisotropy Vector: A Threshold-Free Characterization of Local Structure in Amorphous Materials. *Phys. Rev. Lett.* **2016**, *116* (8), 1−5.
(62) Konstantinou, K.; Mocanu, F. C.; Lee, T. H.; Elliott, S. R. Revealing the Intrinsic Nature of the Mid-Gap Defects in Amorphous Ge2Sb2Te5. *Nat. Commun.* **2019**, *10* (1), 3065 DOI: 10.1038/s41467-019-10980-w.
(63) Riffet, V.; Vidal, J. Statistics-Based Analysis of the Evolution of Structural and Electronic Properties of Realistic Amorphous Alumina During the Densification Process: Insights from First-Principles Approach. *J. Phys. Chem. C* **2017**, *121* (44), 24745−24758.
(64) Sabino, F. P.; Besse, R.; Oliveira, L. N.; Wei, S. H.; Da Silva, J. L. F. Origin of and Tuning the Optical and Fundamental Band Gaps in Transparent Conducting Oxides: The Case of M_2O_3(M = Al,Ga,In). *Phys. Rev. B - Condens. Matter Mater. Phys.* **2015**, *92* (20), 1−7.
(65) Filatova, E. O.; Konashuk, A. S. Interpretation of the Changing the Band Gap of Al2O3 Depending on Its Crystalline Form: Connection with Different Local Symmetries. *J. Phys. Chem. C* **2015**, *119* (35), 20755−20761.
(66) Ghuman, K. K. Mechanistic Insights into Water Adsorption and Dissociation on Amorphous -Based Catalysts. *Sci. Technol. Adv. Mater.* **2018**, *19* (1), 44−52.
(67) Duarte, V. S. S.; Rodrigues, A. M.; de Andrade-Filho, T. S.; Souza, D. do N.; de Novais, E. R. P.; Novais, A. de L. F.; de Oliveira, G. C. A. Structural and Electronic Properties of Amorphous Bismuth Calcium Borate from First-Principle Calculations. *Struct. Chem.* **2021**, *32* (4), 1589−1595.
(68) Triana, C. A.; Araujo, C. M.; Ahuja, R.; Niklasson, G. A.; Edvinsson, T. Disentangling the Intricate Atomic Short-Range Order and Electronic Properties in Amorphous Transition Metal Oxides. *Sci. Rep.* **2017**, *7* (1), 2044 DOI: 10.1038/s41598-017-01151-2.
(69) Mora-fonz, D.; Kaviani, M.; Shluger, A. L. PHYSICAL REVIEW B 102, 054205 (2020) Disorder-Induced Electron and Hole Trapping in Amorphous TiO 2. *Phys. Rev. B* **2020**, *102* (5), 54205.
(70) Pham, H. H.; Wang, L. W. Oxygen Vacancy and Hole Conduction in Amorphous TiO2. *Phys. Chem. Chem. Phys.* **2015**, *17* (1), 541−550.
(71) Mora-fonz, D.; Kaviani, M.; Shluger, A. L. Disorder-Induced Electron and Hole Trapping in Amorphous TiO 2. *Phys. Rev. B* **2020**, *102* (5), 54205.
(72) Subedi, K. N.; Prasai, K.; Kozicki, M. N.; Drabold, D. A. Structural Origins of Electronic Conduction in Amorphous Copper-Doped Alumina. *Phys. Rev. Mater.* **2019**, *3* (6), 1−9.
(73) Dicks, O. A.; Cottom, J.; Shluger, A. L.; Afanas'Ev, V. V. The Origin of Negative Charging in Amorphous Al 2 O 3 Films: The Role of Native Defects. *Nanotechnology* **2019**, *30* (20), 205201.

https://doi.org/10.1021/acsomega.2c04402
ACS Omega 2022, 7, 41033−41043